

# Effect of modeling method on prediction of cortical bone strength adaptation under various loading conditions

C.S. Florio · K.A. Narh

Received: 27 August 2011 / Accepted: 14 September 2012 / Published online: 9 October 2012  
© Springer Science+Business Media Dordrecht 2012

**Abstract** The ability to numerically simulate the effects of different loading conditions on the strength adaptation of a bone can be a valuable tool in understanding the relationship between the strength of a bone and its mechanical environment. Because significant strength changes may result from alterations in the profile of the surface of cortical bone, many computational models of bone strength adaptation have been developed to predict load-induced shape modifications. To gain insight into the effects of the modeling methods used for these predictions, the resulting changes to the surface profile of an initially circular cylinder were compared for a number of computational modeling methods. Models based on strain tensor, von Mises stress, and strain energy density were examined under various loading conditions including axial, bending, torsional, and surface forces as well as combinations of these basic loading modes. The differences between the use of a singular reference value and the use of a range of reference values to drive the magnitude of the local shape changes were investigated. Trends in the strain distributions were analyzed. The comparisons performed indicated that, despite the high sensitivity to the values of the model parameters used under the applied loading modes, with

the proper selection of these parameters, the diverse methods studied yielded quite similar predictions of the bone's shape changes, and thus, strength adaptations.

**Keywords** Cortical bone · Strength adaptation · Computational modeling · Loading modes

## List of symbols

### Vectors

- $\vec{F}_i$  Dimensionless force vector at node  $i$  in “spring-based” smoothing method, Eq. (2a)
- $\vec{x}_i$  Location of node  $i$ , Eq. (2b)
- $\Delta\vec{x}_i$  Displacement at node  $i$  in spring smoothing method, Eq. (2a)
- $\Delta\vec{x}_j$  Displacement at node  $j$  in spring smoothing method, Eq. (2a)
- $k_{ij}$  Effective spring constant for element edge connecting nodes  $i$  and  $j$  in spring smoothing method. Dimensions of  $1/[L]$ , Eq. (2a)

### Scalars

- $d_{ij}$  Distance between nodes  $i$  and  $j$ , Eq. (4)
- $diff_i$  Difference between strain at node  $i$  and reference strain for node  $i$ , Eq. (3a)
- $DINFL$  Characteristic distance between nodes over which the effect of the growth at one node on the growth at other nodes is scaled by  $1/e$ , Eq. (4)

---

C.S. Florio (✉) · K.A. Narh  
Department of Mechanical and Industrial Engineering,  
New Jersey Institute of Technology, Newark, NJ 07102,  
USA  
e-mail: cxf6791@njit.edu

$G_i$	Growth at node $i$ , Eq. (3a)
$NW$	Circumferential smoothing weighting factor, Eq. (4)
$W_{axial}$	Axial smoothing weighting factor, Eq. (6)
$W_{rate}$	Rate factor that scales the growth per load application iteration, Eq. (3a)
$i, j, k, n$	indices
<i>Greek</i>	
$\varepsilon_i(n)$	$n$ th strain tensor component for node $i$ . Strain tensor defined as engineering strain transformed into the local cylindrical coordinates for each node $i$
$\varepsilon_{ref\ max}(n)$	Max value of reference range for $n$ th strain tensor component
$\varepsilon_{ref\ min}(n)$	Min value of reference range for $n$ th strain tensor component
$\sigma_{VM}^{iAVG}$	Numerical average of the nodal von Mises stresses of the nodes located on the same surface (inner or outer) as node $i$ that have the same local $z$ -coordinate as node $i$ , Eq. (6)
$\sigma_{VM}^{midAVG}$	Numerical average of the nodal von Mises stresses of nodes located on same surface as node $i$ (inner or outer) and at the midplane (local $z$ -coordinate of this set of nodes = local $z_{max} - \text{local } z_{min}$ ) of the cylindrical geometry studied, Eq. (6)

## 1 Introduction

As a living tissue, bone has the ability to adapt its strength to suit its mechanical environment. This is done through modifications of both its intensive and extensive properties. Intensive property changes in a bone are related to the mineral content of the material comprising the bone or “bone density”. Extensive property changes are related to alterations in the bone geometry: the size or shape of the overall volume of the bone.

While these changes occur in all types of bones, the adaptations in long bones are of significant importance, as long bones support the largest forces and are key to most activities. In adults, the adaptation of the extensive properties of long bones occurs through accretion or removal of material on the periosteal (outer) and endosteal (inner) surfaces of the diaphyseal (mid-shaft) region of cortical tissue located near the surface

of the bones. Adaptation of the intensive properties occurs mainly through modifications in the concentration of the minerals that are stored in the cancellous bone tissue at the interior of the ends of long bones [1].

Both intensive and extensive property modifications in a bone can impact its mechanical strength through changes in material properties and shape, respectively. However, strength of materials relations show that modifications to the cross-sectional shape have the potential to result in larger improvements in the mechanical strength of the region of change than an equal amount of change in material density at this local region. This concept is employed naturally by living tissues, including bone, when strength modifications are necessary. For example, a fracture callus, which is a large bulbous structure made of a weaker material than standard cortical bone tissue, quickly forms around the outer surface of a broken region of bone, increasing the local cross-sectional area. This fracture callus stabilizes the fracture while the more intensive long-term fracture healing and remineralization processes occur [1]. Additionally, the inner and outer diameters of the long bones in the diaphyseal region naturally increase to improve the regional mechanical strength, countering the typical loss of material strength associated with decreased bone mineralization, and thus density, that occurs with age [2].

While changes in intensive material properties in local bone density are chemically motivated transient phenomena that are related to the bone’s role as a reservoir for minerals that are used by a number of other systems [1, 3], the extensive property (geometric) changes in the local shape may result in more substantial and stable changes in bone strength. Thus, the ability to predict the extensive property (shape) changes in long bones as a function of local loading conditions can be a valuable tool in improving the understanding of bone strength adaptation. Computational methods offer the additional advantage of allowing for more quantitative comparisons of the effects of environmental parameters under more controlled conditions with greater efficiency than experimental or clinical studies.

The goal of this work is to examine the effects of the method of modeling cortical bone adaptation on the prediction of changes to the shape of an initially circular three-dimensional cylinder under various basic axial, bending and torsional loading modes and combinations of these modes. Because strength

changes are directly related to shape changes, this will lead to the development of a computational modeling technique that may be used to directly compare the effects of different loading conditions on the changes in the strength of a long bone.

## 2 Related work

Numerous computational models have been developed over the past forty years to predict the shape changes in long bones as a result of alterations in the mechanical environment.

Most of these computational models share a fundamental simulation method [4–11] which follows the general format of:

$$Growth_i \propto (Measure_i - Measure_{reference}) \quad (1)$$

In these methods, measures of the local mechanical state are calculated either through finite element or boundary element methods. These local measures are a function of the stress and/or strain at surface nodes, elements, or keypoints. The local measures are then compared to reference values. These reference values can be local, regional or global and represent a “steady state” or “equilibrium state” at which no shape changes occur. The reference values are related to the “typical” loading conditions encountered by the bone. To simulate the bone material apposition or resorption, the locations of the local points in the computational model defining the boundary surfaces are then moved in proportion to the difference between the local measure and the reference value. This process is repeated until convergence or another like goal is attained. Because bone adaptation in adults is considered in this study, only cross-sectional shape changes, and no longitudinal or axial changes, are considered.

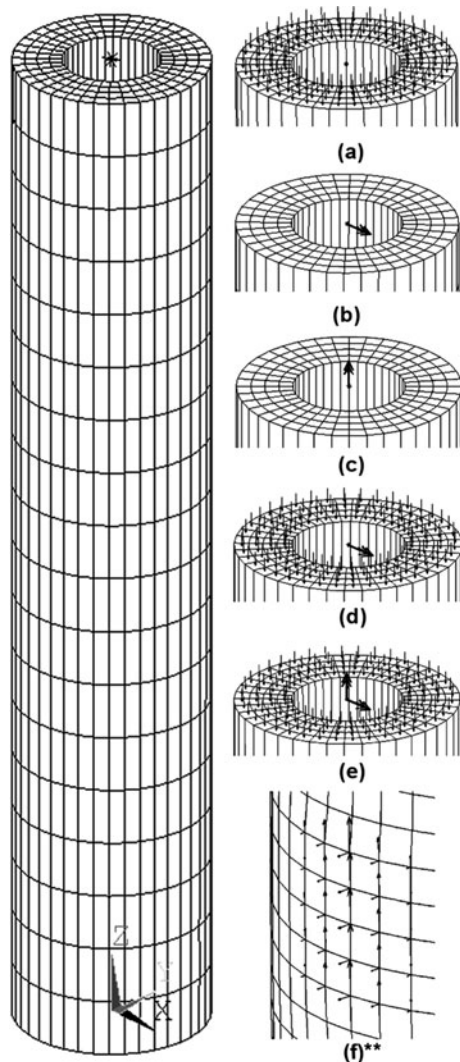
The differences in modeling methods are mainly related to the choice of the local measure used to drive the adaptation simulation. These local measures are used to describe the local mechanical state on the surface of the geometry of interest. Some modeling methods are based on the stress or strain tensors [4, 12–15] or their gradients [16, 17]. These methods allow for the separation of the effects of individual tensor components (normal and shear) and can account for the effects of loading direction. Therefore, each component of the stress or strain tensor may have a different effect on the local shape changes through the selection of individual model parameters. Other modeling

methods consider the combined effects of these tensor components through the use of averaged stress and/or strain measures. These models are driven by measures such as strain energy density (SED), von Mises stress, principal strains or stresses or gradients of these values [7, 8, 11, 18, 19]. While these methods cannot control the growth effects separately for each individual tensor component, they are often easier to implement because they eliminate both the need to track directionality and the need to determine reference values for each tensor component, since averaged values can be more readily estimated.

Despite the abundance of models developed, their application to the study of actual systems has been limited. Some model validations to experimental results have been published [5, 9, 10, 20, 21]. Additionally, studies have been performed to explore the effects of variations in model parameters such as the specified reference values and growth rates [5, 7, 13, 14, 20, 22]. Few, however, have proceeded to apply these models to study or compare the effects of specific loading conditions.

The present work will analyze the effects of two basic features common to these computational bone shape adaptation methods: the description of the measure reference driving the amount of change and the choice of the driving measure itself, on the prediction of the shape changes under various loading conditions. Shape changes considered in this model will only consider the cortical region of the mid-shaft of a long bone.

In the first phase of this study, comparisons will be made between the use of a singular point reference value and a reference that spans a range of values. A simple hollow cylindrical volume, as shown in Fig. 1, will be used to carry out the study with an applied bending load. For the single point reference value, there is a single threshold value above which local material accretion is simulated and below which local material removal is simulated [11, 12]. If the local measure is equal to the threshold value, no changes occur. When the reference spans a range of values, no changes occur while the local driving measure is within this reference range. Material removal (decay) occurs only when the measure is less than the lower limit of this range and accretion (growth) occurs only when the local measure is greater than the upper limit of this reference range. The range of reference values has been called a “Lazy Zone” or “Equilibrium Zone”



\*\*Mesh modified to allow surface force application over a small area

**Fig. 1** Geometry and loading cases studied: (a) Axial, (b) Bending, (c) Torque, (d) Axial + bending, (e) Axial + bending + torque, (f) Bending + torque + surface force

and has been used in previously developed models to represent the range of loading conditions that occur during activities of daily living [8, 23, 24]. As a result, in these reference range-type models, the threshold value that triggers regional material removal or decay is different from the one that triggers the regional addition of bone material or growth.

In the second phase of this study, the influence of the driving measure is analyzed. A strain tensor based driver measure [12–14] is used in the devel-

oped model and comparisons are made to published results for models using various reference measures and reference types. The system in these investigations is an initially circular three-dimensional cylinder under axial, bending, torsional, and surface loads as well as combinations of these basic loading modes. The resulting changes to this geometry under the studied loads are compared to published changes of a three dimensional geometry using a von Mises stress based model with a point reference value [11] and of a two-dimensional geometry using a strain energy density based model with a reference spanning a range of values [23]. While these reference publications depict the effect of loading mode on bone growth using von Mises stress and strain energy density based models respectively, little similar published data was found for a strain tensor based growth driver model. Thus, such a model was developed in this current study as a means to compare the three basic driver measures used in many cortical bone adaptation models. Comparisons of the resulting geometries are also made to published representations of typical cross sectional geometries of actual bones [25, 26].

The insight gained through these two phases of study will allow for a better understanding of the effects of the selection of modeling methods and parameters on the prediction of the shape adaptation as well as the effects of basic loading modes on the strength changes of the cortical mid-shaft region of long bones.

### 3 Methods

To carry out these investigations, a finite element analysis method was implemented. All analyses were performed using ANSYS 11.0 [27]. User defined subroutines were written in Fortran to apply the shape adaptation model and to perform node smoothing as the shape is altered. The application of the model parameters, the execution of the analyses, and the control of the iterative load application and analyses were handled through the creation of an executable script written in the ANSYS Parametric Design Language (APDL). The application of the load, solution of the static finite element analysis, adaptation of the boundary surface shape, and subsequent node smoothing were performed iteratively for a prescribed number of cycles or until a convergence measure was achieved. Details are provided below.

### 3.1 Geometry and basic finite element model

A three-dimensional initially circular hollow cylinder was created with an inner diameter of 15 mm, an outer diameter of 30 mm, and a length of 160 mm (Fig. 1). It was assigned linear elastic isotropic material properties with an elastic modulus of 20 GPa and a Poisson’s ratio of 0.3. The geometry was meshed with 8-node hexahedral elements. This allowed for the creation of a regular mesh with a uniform radial, circumferential and axial element sizes throughout the geometry. No midside nodes were used so that the inner and outer radial surfaces could be moved freely, solely by changing the positions of the corner nodes. As with the geometric dimensions and material properties, the element sizes were chosen based on the published articles used for comparison [11, 23]. By eliminating the variations between geometry, material properties and mesh among the models compared, the effects of the shape adaptation model used can be more easily identified.

Figure 1 shows the initial meshed hollow cylindrical geometry used for this study and the loading conditions investigated. The element sizes used match those in [11]. The bottom surface ( $Z = 0$  m) was completely constrained in all degrees of freedom. All other surfaces were free. The loads were applied to the top surface ( $Z = 0.160$  m) through the use of surface elements or a contacting centroidally located pilot node. For the case with the applied surface forces, simulating the pull of a muscle on the bone, forces were distributed over small regions on the outer surface of the cylindrical geometry that were sized to represent tendon attachment areas. A simple circular cylindrical geometry was chosen as the initial shape in these studies because it allowed for ease of comparison and because this simplification is widely used to represent the mid-shaft region of long bones [11, 23, 28–30].

The shape adaptations resulting from the local loading conditions were simulated through the movement of the inner and outer surface nodes in a local radial direction (normal to the surface at each node). To maintain the integrity of the mesh, two types of nodal smoothing were devised. The first type of smoothing was of the nodes on the interior of the volume of the geometry. The interior smoothing was done to maintain consistent element sizes between the interior elements and the exterior elements, where growth or decay occurs, in order to prevent element distortion. The

second type of smoothing was performed on the exterior surface nodes. This smoothing reduces the potential for element distortion in areas of high stress concentrations and the resulting isolated areas of large amounts of growth.

Smoothing on the boundary surface was handled in two separate directions to distribute the local nodal shape change effects to neighboring nodes. These smoothing methods were incorporated directly into the shape adaptation model at each load application iteration and are further discussed in Sect. 3.2.

Interior node smoothing was performed using an equivalent “spring-based” method [31]. In this method, the mesh system of connected nodes is represented as a system of connected linear springs. At the initial nodal positions, before any surface shape adaptation occurs for the load application iteration, the spring system is in equilibrium. As the adaptation simulation moves the surface nodes, dimensionless “spring forces” proportional to the displacement along the imaginary springs connected to the surface nodes are generated following a dimensionless form of Hooke’s law. The forces are propagated through the interior connections as shown in Eq. (2a).

$$\vec{F}_i = \sum_j^{n_i} \mathbf{k}_{ij}(\Delta\vec{x}_j - \Delta\vec{x}_i) \tag{2a}$$

where  $n_i$  = number of neighboring nodes connected to node  $i$ .

The effective spring constant is defined as:

$$\mathbf{k}_{ij} = \frac{1}{\sqrt{(\vec{x}_i - \vec{x}_j) \cdot (\vec{x}_i - \vec{x}_j)}} \tag{2b}$$

Thus, the effective spring constant is inversely proportional to the magnitude of the pre-smoothed distance between neighboring nodes  $i$  and  $j$  before the surface nodes were moved by the shape adaptation model in the given iteration.

With the displacement of the outer nodes known from the shape adaptation model, the displacements of the interior nodes required to create more uniform element sizes are calculated through a system of equations patterned after force equilibrium equations for a system of connected linear springs between connected nodes. In this way, the interior nodes are moved in a manner proportional to the shape adaptation model predicted changes in the positions of the inner and outer surface nodes, denoted  $\Delta\vec{x}_1$  and  $\Delta\vec{x}_N$ , respectively.



Because of the regular hexahedral mesh and the assumption of no axial bone growth in this model, the shape adaptation simulation causes only local radial changes in the positions of the surface nodes. Thus, the movement of each surface node only affects the interior nodes along radial lines and so the system becomes a one-dimensional set of springs. Thus, in applying Eq. (2a) to the mesh in this study,  $n_i = 2$  for interior nodes and  $n_i = 1$  for surface nodes. The coefficient matrix in the system of force equilibrium equations in (2a) is reduced to a simple band matrix.

Since the application of the interior node smoothing method over the entire volume studied can be computationally intensive, especially for finer meshes, and because small amounts of change to surface node positions at the majority of the surface nodes typically occur with each load application iteration, this smoothing was performed only once every five load application/boundary surface shape modification iterations.

### 3.2 Developed shape adaptation model

While three basic model driver measures: strain tensor, von Mises stress and strain energy density, were compared in the second phase of this work, only one, the strain tensor, was chosen for the numerical model developed in this work for the current investigation and used in the first phase study of the effect of reference type. This developed model will be described in detail. Details on the other shape adaptation modeling methods used for comparison can be found in [11, 23].

The use of the nodal strain tensor component values to modify the nodal positions on the outer and inner surface boundaries has been widely used [12–14]. In this type of model, the strain tensor components at each node are found and individually compared to reference values. The individual effects of these components are summed for each node to determine the total amount of change in the position of that node.

Two major modifications to this basic model were made in the current work. First, the nature of the strain tensor component based models requires a method to eliminate the effect of the direction of the torsional loads on the direction of growth. (For example, because strain tensor based models compare magnitudes as well as directions of the nodal measures to those of selected references, a positive torque might create growth while a negative torque might cause decay. Thus, the models prediction of shape change

would artificially be affected by the arbitrary selection of the direction of torque application.) Early models handled this by squaring shear strain components, thereby making all shear strains produce material addition/growth. This squaring also resulted in a reduction of the order of the effect of torsional loads, as it was thought that typical torsional loads were much smaller than typical bending loads in long bones [14]. However, because long bones, such as the femur, actually can carry a significant torsional load [32–36], in the model developed in the current work, their importance related to the amount of shape change was weighted the same as that of normal loads. This is shown by the use of the same order for all strain tensor component comparisons in the growth model (3a). The elimination of the effect of torsional direction was accomplished through the use of the absolute value of the difference between the nodal shear strain values and shear strain reference values. The direction of the growth was then assigned based on the comparison of the magnitude of the nodal shear strain component to the magnitude of the shear strain component reference. This method allowed small torsional loads compared to the chosen reference threshold values to produce decay, just as those in the normal directions.

The basic model for growth,  $G$ , at node  $i$  used in the developed model is shown in (3a).

$$G_i = W_{rate} \sum_{n=1}^6 \text{diff}_i(n) \quad (3a)$$

where

$$\text{diff}_i(n) = \varepsilon_i(n) - \varepsilon_{ref}(n) \quad (3b)$$

(Note:  $G_i > 0 \rightarrow$  growth,  $G_i < 0 \rightarrow$  decay.)

Depending on the user's preference,  $W_{rate}$  can represent a particular rate of growth related to the load application iteration at a particular location or can be arbitrarily chosen to efficiently achieve convergence.

The term  $\text{diff}_i(n)$  in (3a) is the driving mechanism behind the shape adaptation model. The six local engineering strain component values  $\varepsilon_i(n)$  that are used in the six terms of the sum in Eq. (3a) allow each strain component to have a different corresponding reference value. The variable  $\text{diff}_i(n)$  was determined from the following constraints for cases where the minimum and maximum threshold values of a range reference are of the same sign.

$$\mathbf{IF} \left[ \begin{array}{l} [|\varepsilon_i(n)| > |\varepsilon_{ref\ max}(n)|] \ \mathbf{and} \\ [\text{sign}(\varepsilon_{ref\ max}(n)) = \text{sign}(\varepsilon_i(n))] \end{array} \right]$$

$$\text{diff}_i(n) = \varepsilon_i(n) - \varepsilon_{ref\ max}(n)$$

resulting in a positive value for  $\text{diff}_i(n)$  so that strain component contributes to growth.

$$\mathbf{IF} \left[ \begin{array}{l} [|\varepsilon_i(n)| < |\varepsilon_{ref\ min}(n)|] \ \mathbf{and} \\ [\text{sign}(\varepsilon_{ref\ min}(n)) = \text{sign}(\varepsilon_i(n))] \end{array} \right]$$

$$\text{diff}_i(n) = \varepsilon_i(n) - \varepsilon_{ref\ min}(n)$$

resulting in a negative value for  $\text{diff}_i(n)$  so that strain component contributes to decay.

$$\mathbf{IF} [|\varepsilon_{ref\ min}(n)| \leq |\varepsilon_i(n)| \leq |\varepsilon_{ref\ max}(n)|]$$

$$\text{diff}_i(n) = 0.0$$

resulting in neither growth or decay.

Similar logic would follow to determine expressions for  $\text{diff}_i(n)$  if the minimum and maximum threshold values of the reference range are of different signs. Likewise, the computations needed to find  $\text{diff}_i(n)$  can be reduced if the minimum and maximum reference threshold values are equal, resulting in a singular point reference, as was done in Phase 1 of this study.

The second major modification to the basic strain tensor based model involves the inclusion of surface smoothing. Surface node smoothing was added directly within the basic model described in (3a) through the inclusion of two weighting factors so that the calculated local nodal growth at each load application iteration was directly related to the growth at surrounding nodes, allowing for more gradual transitions in amounts of growth between regions of varying strain. Two surface node smoothing methods were employed: circumferential smoothing and longitudinal (axial) smoothing. The development and implementation of each is now described in detail.

The circumferential surface nodal smoothing method simulated the communication between mechanoreceptor cells in the cortical bone and was based on a model developed for a similar communication in cancellous bone [37]. These cells communicate through fixed channels (cannaliculi) in the bone material. In this model, the changes at each node affect the changes at nearby nodes by an exponentially decreasing relation to the distance between the nodes. Thus, the growth at a node is the sum of the effects of all other

nodes multiplied by a weighting factor,  $NW_j$ , defined in (4):

$$NW_j = e^{-(d_{ij}/DINFL)} \tag{4}$$

where node  $i$  is the node for which growth is being calculated and node  $j$  is the nearby node. In preliminary studies using the currently developed model, the relationship between nodal growth and the chosen value of the range of influence,  $DINFL$ , in (4) was cubic, with the inflection point at a value of  $DINFL$  equal to approximately twice the average distance between nodes. Thus, the reference distance  $DINFL$  in the circumferential smoothing method was given a value of twice the average distance between nodes in the studies described here.

Published studies have found that most of the “communication channels” are oriented in the cross-sectional plane of the long bone and few are oriented axially [38–40]. Therefore, the circumferential smoothing in this model considered only the nodes in the same axial plane that are on the same surface (inner or outer). Thus, the modified model becomes (5):

$$G_i = W_{rate} \left[ \sum_{j=1}^k NW_j \left( \sum_{n=1}^6 \text{diff}_i(n) \right)_j \right] \tag{5}$$

where  $k$  is equal to the number of nodes on the same surface as node  $i$  that have the same local axial ( $z$ ) coordinate value as node  $i$  (are coplanar).

The axial (longitudinal) surface nodal smoothing model was developed to address the effects of the boundary conditions on local stress/strain concentrations near the loaded and constrained surfaces. Because the amount of nodal growth (or decay) is directly related to the nodal strain tensor, locally high strains related to the boundary conditions could create abnormally large amounts of nodal growth or decay. The influence of the boundary conditions on the amounts of growth or decay diminishes with distance from the loaded or constrained surfaces. Therefore, the growth at each node was further modified by an axial smoothing factor for each node,  $(W_{axial})_i$ , given in (6):

$$(W_{axial})_i = \left( \frac{\sigma_{VM}^{MidAVG}}{\sigma_{VM}^{iAVG}} \right)^2 \tag{6}$$

This quadratic factor scales the growth of node  $i$  in proportion to the ratio between the stresses at the mid-plane of the cylinder, a location away from loading surfaces,  $\sigma_{VM}^{MidAVG}$ , and the stresses in the vicinity of node  $i$ ,  $\sigma_{VM}^{iAVG}$ , thus reducing the amount of growth that

would occur due to the high stresses resulting from the boundary effects.

Therefore, the final strain tensor driven shape adaptation model which directly includes surface node smoothing is given by (7):

$$G_i = W_{rate}(W_{axial})_i \left[ \sum_{j=1}^k NW_j \left( \sum_{n=1}^6 \text{diff}_i(n) \right)_j \right] \quad (7)$$

### 3.3 Model analysis phase 1: point vs. range reference

The first phase of the analysis considered the effect of the type of reference used in the shape adaptation model. The effect of a single point reference value versus a reference that spanned a range of values (“lazy zone” or “equilibrium zone”) was compared for the system loading case shown in Fig. 1b. The analysis was performed using the author-developed model described in Sect. 3.2 for the same geometric and bending load conditions as studied in [11], which used a point reference and a von Mises stress driven model. Depictions of the relationships between the amount of growth and strain tensor component value used for the point reference and the reference range are shown in Figs. 2a and 2b, respectively. The slopes of these “growth curves” are equal to  $W_{rate}$  in (7) and can vary based on location and/or direction of shape change (growth or decay) or can be held constant, as in this model.

The loading values were chosen to match those in [11] with a bending moment of 100 N mm. The threshold values matched those of [11] with a 0.02 MPa reference von Mises stress. Because the current model used strain tensor components, it was not possible to find corresponding reference values for all the strain tensor components. Therefore, the strain corresponding to the 0.02 MPa stress for the material properties chosen, or  $\pm 1.0\mu\epsilon$ , was used as the reference for each strain tensor component for the point reference value. For the reference range, the threshold limits were arbitrarily chosen to be  $\pm 50\%$  of the point reference values so that the growth thresholds ( $\epsilon_{ref\max}$ ) were ( $\pm 1.5\mu\epsilon$ ) and the decay thresholds ( $\epsilon_{ref\min}$ ) were ( $\pm 0.5\mu\epsilon$ ).

Models were run for an arbitrary number of iterations until growth at the midplane appeared to reach a constant value or until the wall thickness reached a cutoff value, chosen to prevent element collapse. Quantitative comparisons of each of the strain tensor

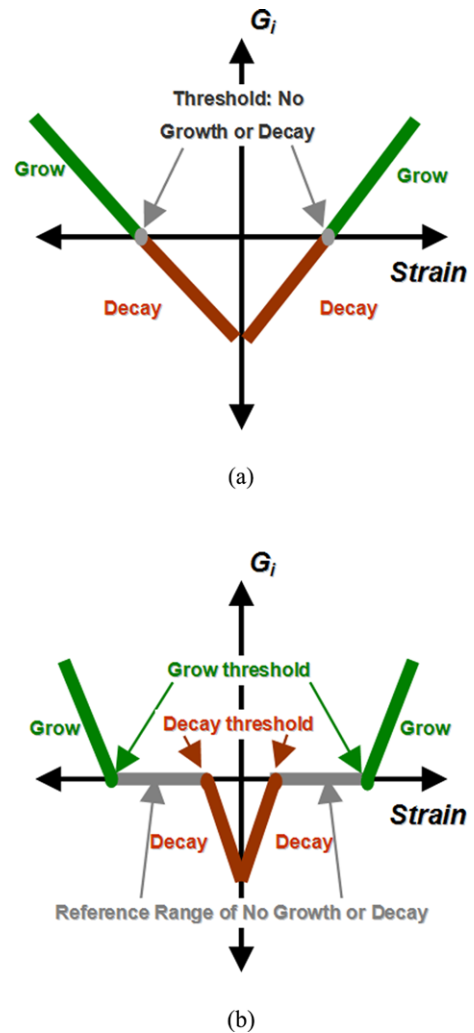


**Fig. 2** Relationship between growth and strain for (a) Point reference model, (b) Range reference model

values at the midplane for the inner and outer surface at angular coordinates of  $0^\circ$ ,  $45^\circ$ , and  $90^\circ$  were made between the models with these two types of references. Qualitative comparisons were made between the resulting cross sectional geometries and von Mises strain distributions.

### 3.4 Model analysis phase 2: comparison of model driver measures

In the second phase of this analysis, the effect of the growth driver was investigated and compared to published results for various loading conditions. The developed strain tensor driven model was used to predict shape changes under the six loading conditions listed



**Table 1** Comparison of geometry and finite element models used

	Current Model (Strain Tensor Based)	von Mises Stress Based Model [11]	SED Based Model [23]
Dimensions	3-D	3-D	2-D
Initial ID	15 mm	15 mm	18 mm
Initial OD	30 mm	30 mm	30 mm
Length	160 mm	160 mm	Infinite
Material Model	Isotropic	Isotropic	Transversely Isotropic
Method of Shape Modification	Move surface nodes by calculating radial change	Move surface nodes by calculating simulated volumetric swelling strain	Move surface nodes by calculating radial change. Fit new cubic spline to boundaries
Stopping Criteria	Constant, near constant or zero amount of change in nodal position per iteration	Number of iterations or a certain % reduction in max von Mises Stress	Constant, near constant, or zero amount of change in nodal position per iteration
Method of Mesh Smoothing	Interior node smoothing every 5 iterations; surface smoothing every iteration	Interior node smoothing only every iteration	Complete remesh every iteration
Mesh Type	Mapped uniform Hexahedral Elements	Mapped uniform Hexahedral Elements	Graded Mapped Quadrilateral Elements—smaller elements near Outer Diameter (OD)

in Fig. 1. Reference [11] provided the predicted shape changes for a von Mises stress driven model used for comparison in this study. Those for the strain energy density driven model in [23] were likewise used for comparison. Additional qualitative comparisons were made to published images of cross sectional geometries of transverse slices through actual femur bones [11, 25, 26]. While the basic geometric and loading characteristics were the same for each model compared, specific differences are shown in Tables 1 and 2.

Although the relative axial, bending and torsional loads typically applied to a femoral bone, the structure simulated in this investigation, were used as a guide in the selection of the loading values in these studies, the investigation was not intended to represent any specific activity or condition. While the main mode of loading in the human femoral bone results from bending, axial compression and torsion also play significant roles, as the stresses due to axial compression, bending and torsional loads typically occur at a ratio of 1:8:2 [32–36]. Additionally, because muscles produce some of the largest forces exerted on a bone [3], the study of the muscle force influence is warranted and simulated

through the addition of the surface force loading case depicted in Fig. 1f.

Loading conditions were selected to match those in the publications used for comparison of shape changes for the different model drivers. The loading values in all of the cases studied using the developed strain tensor based model were based on those used in Ref. [11], the von Mises stress based model, because this reference was chosen as a basis for the three-dimensional geometry and applied material properties used in the developed model. The loading values used by Ref. [23], the strain energy density based model, were generally two to three orders of magnitude more than those used in Ref. [11], and the authors of the SED study selected the loads to be twice the value at the midpoint of a constant range reference. Especially with the differences in the loading values between the studies compared, care was taken in selecting the parameters in the current study to ensure that the relative amounts of stress on the bone volume resulting from each of the basic loading modes, as well as ratios between the reference threshold values and applied loading values, were similar to the published papers used

**Table 2** Comparison of load application methods used for the loading modes studied

	Current Model (Strain Tensor Based)	von Mises Stress Based Model [11]	SED Based Model [23]
<b>Axial</b>			
Method of Load Application	Pressure applied to elements on top surface	Axial force on top surface	Centroidally applied force at a point
$\frac{\text{Reference Threshold}}{\text{Applied Load}} \%$	25–75 %	100 %	30–70 %
<b>Bending</b>			
Method of Load Application	Moment on pilot node in contact with top surface elements	Moment applied to top surface	Seven equal magnitude moments about axes equally distributed over 90° sector
$\frac{\text{Reference Threshold}}{\text{Applied Load}} \%$	50–500 %	50 %	30–70 %
<b>Torsion</b>			
Method of Load Application	Moment on pilot node in contact with top surface elements	Moment about cylindrical axis	Centroidally applied torque
$\frac{\text{Reference Threshold}}{\text{Applied Load}} \%$	100–1000 %	100 %	30–70 %
<b>Axial + Bending</b>			
Method of Load Application	Combination of above	Combination of above	Seven equal magnitude offset axial loads equally distributed over 90° sector
Stress Ratio	A:B = 1:2	A:B = 1:2	A:B = 1:4.6
$\frac{\text{Reference Threshold}}{\text{Applied Load}} \%$	33–333 %	33–100 %	Unknown: “[load] greater than twice mid-reference range”
<b>Axial + Bending + Torsion</b>			
Method of Load Application	Combination of above	Combination of above	Seven equal magnitude offset axial loads equally distributed over 90° sector + centroidally applied torsion
Stress Ratio	A:B:T = 1:2:1	A:B:T = 1:2:1	A:B:T = 1:4.6:1.2
$\frac{\text{Reference Threshold}}{\text{Applied Load}} \%$	33–333 %	33–100 %	Unknown: “produced an initial average periosteal stimulus greater than twice mid-reference range”
<b>Bending + Torsion + Surface Force</b>			
Method of Load Application	Combination of above + Graded Force distributed over small area on outer surface	Combination of above + Force on single node of outer surface	N/A
Moment Ratio	B:T:SF = 2:1:2.75	B:T:SF = 2:1:2.75	N/A
$\frac{\text{Reference Threshold}}{\text{Applied Load}} \%$	25–500 %	~300 %	N/A

for comparison. These ratios are reported in the model comparison in Table 2.

The choice of the threshold limits of the reference range used in the current developed model was made, in part, by trial and error during preliminary studies in order to match the basic trends in shape changes that were reported by Refs. [11] and [23]. The published papers used for comparison had different methods for

selecting the magnitudes of their reference threshold values. The von Mises based model in Ref. [11] used the applied axial compression load as the singular point reference value for all cases studied. Thus, the reference value for that study was based on the chosen loading values. The strain energy density based model of Ref. [23] used the same ratio between reference range threshold limits and initial loading condi-

tions for all loading-type cases investigated. Thus, in that study, loads were based on the chosen reference values. In reality, however, the reference values likely are independent of the specific loading conditions and magnitudes, and so the use of constant reference values for all loading cases studied was desired in the developed current model. Yet, because the strain tensor based driver used sums of the effects of each individual tensor component, slightly different reference values were required for different tensor components under different loading modes to achieve shape changes comparable to these published works.

Quantitative comparisons of the strain tensor values, growth (or decay) per load application, and radius values were made on the midplane at discrete locations along outer surface every 45° for the loading cases studied with the current developed model. These comparisons aid in understanding the effect of each of these basic loading modes on the shape changes predicted using a strain–tensor based model.

Using the model developed in the present study, load application and shape change were iteratively repeated until the surface profile closely resembled that of the same loading type in the published studies used for comparison. Often, a constant amount of growth per load application iteration was also approached.

## 4 Results

### 4.1 Phase 1: point vs range reference

For the applied bending load studied (Fig. 1b), the strain tensor driven shape adaptation model in the current work using the point and range reference values chosen for this investigation produced similar general trends in the altering of the surface profile of an initially circular cylinder as shown in Fig. 3. The regions near the maximum strain, at the 90° location on the outer surface, showed the greatest amount of growth. Regions near the bending (neutral) axis where strains are near zero, at the 0° location, showed the most decay. These trends were consistent with the published von Mises stress based model with a point reference [11] as well as the strain energy density based model with a range reference [23]. The circumferential smoothing method applied to the current model created the gradual transition between these two regional extremes resulting in the egg-shaped geometry shown in Fig. 3. This figure also depicts the similar

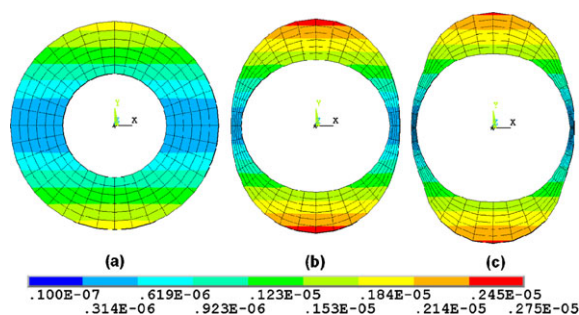


**Fig. 3** Midplane profiles and von Mises strain distributions for (a) Initial, (b) Final-point reference, (c) Final-range reference

**Table 3** Trends in change of radius for different reference types

Location	Inner Surface		Outer Surface	
	Point Ref.	Range Ref.	Point Ref.	Range Ref.
0°	−43 %	−49 %	−19 %	−22 %
45°	−34 %	−48 %	−6 %	−5 %
90°	−27 %	−42 %	3 %	11 %

changes to the von Mises strain distributions from the initially circular cylinder for the two reference types studied and clearly shows the greatest amount of growth near the highest strains. Table 3 shows the change between the initial and final radius values at the 0°, 45° and 90° locations on both the inner and the outer surfaces. Because of the symmetrical geometry and loading about the *x* and *y* axes, these trends also represent the changes at the corresponding locations in the other three quadrants along the boundaries of the geometry studied.

For both the reference point and reference range cases, all model parameters were identical except the values of the reference thresholds. To reach the final shape used for comparison, the point reference model took half the number of iterations of the range reference model. It should be noted that no specific convergence criterion was used to stop these models. The stopping point selected for this comparison for each reference type was simply selected based on visual similarities of resulting shapes.

While the final geometry and final changes in radius were similar for both reference types, the amount of growth resulting from each load application iteration was noticeably different, as represented through the plots of growth per iteration at the 90° location shown in Fig. 4a. At all nodal locations studied,

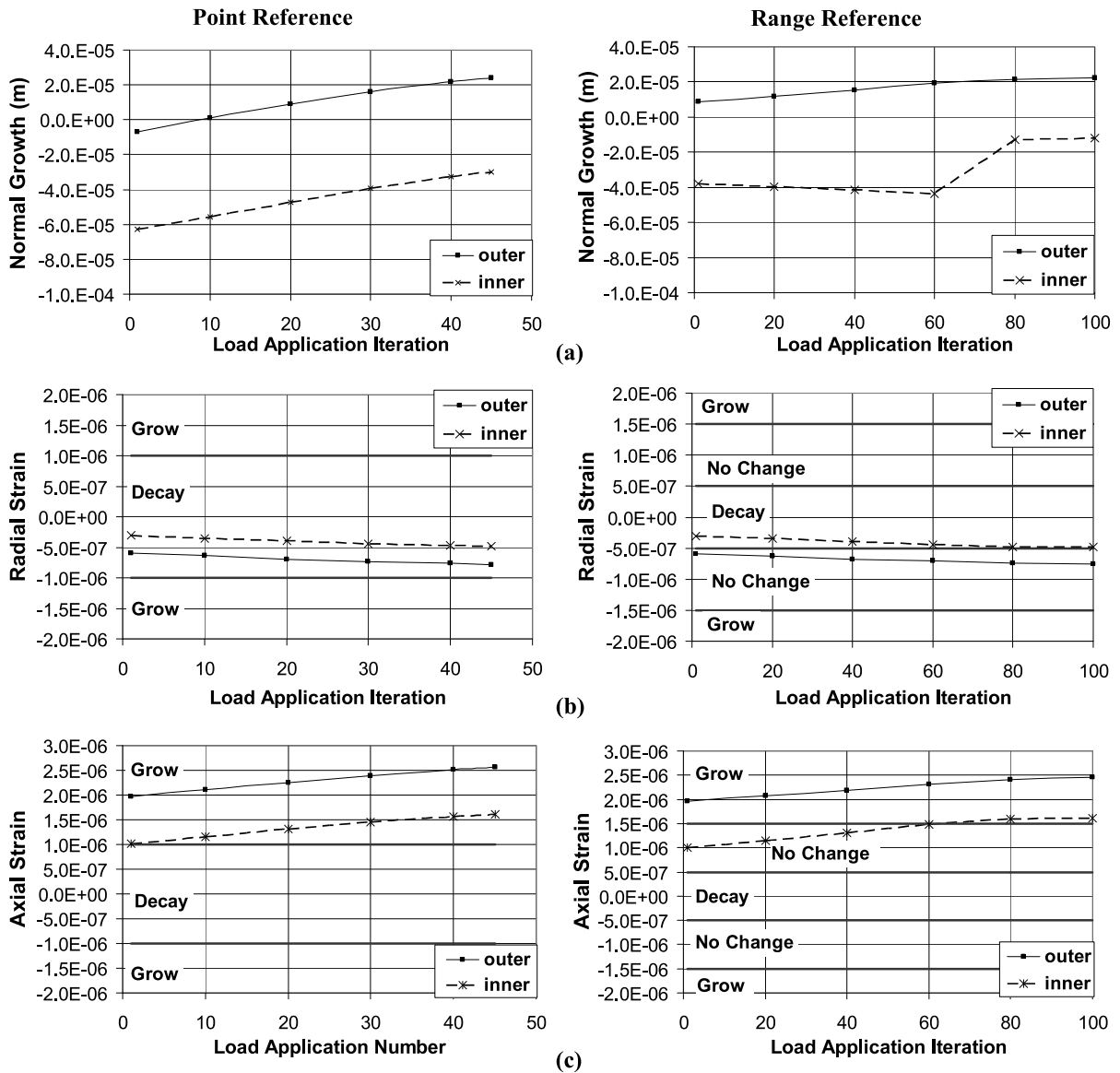


**Fig. 4** Comparison of (a) Growth normal to the inner and outer surfaces, (b) Radial strain, (c) Axial strain with increasing load application iteration during the course of the study at a discrete point ( $\Theta = 90^\circ$ ) for the two reference types examined

the point reference (left column of Fig. 4) showed a smooth trend in growth/iteration with time, with the rate of growth decreasing with iteration. The range reference (right column of Fig. 4), however, showed a discontinuity in the amount of growth per iteration, changing from an increasing rate to a decreasing rate of growth/decay, especially on the inner surface.

Strain tensor component values used in the calculation of the shape change at each iteration at discrete points along the inner and outer surfaces were

also examined. Because of the bending load, the focus of the comparison was on the normal strain components. Radial and tangential normal strains for both reference types at each of the three locations considered were nearly identical. Therefore, only radial and axial strains are presented in Figs. 4b and 4c, respectively. The threshold values are indicated by dark, solid, horizontal lines. The direction of shape change (grow, decay or no change) in each range of strain values is noted and is consistent with the re-

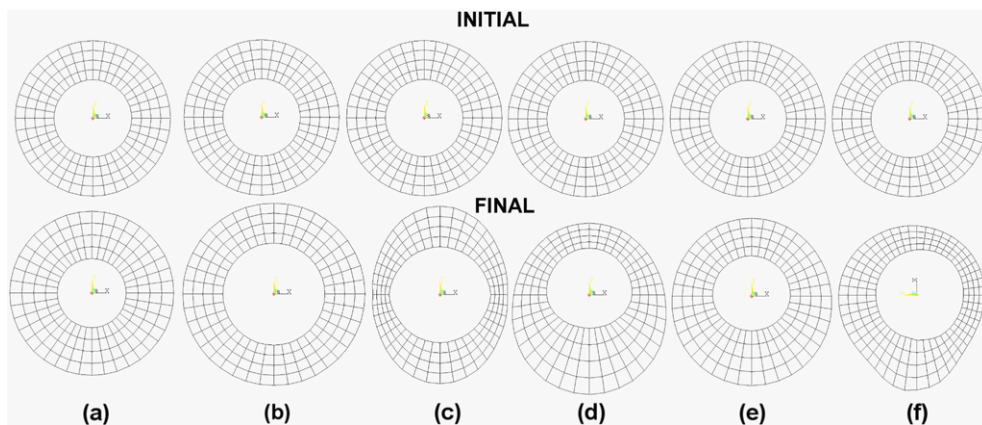


**Fig. 5** Shape resulting from various loading modes using strain tensor model. (a) Axial, (b) Torsion, (c) Bending, (d) Axial + bending, (e) Axial + bending + torsion, (f) Bending + torsion + surface force

gions depicted in Figs. 2a and 2b. For all strain tensor components, strains on the outer surface were greater than strains on the inner surface. However, the axial strains differed more from inner to outer surface than did the radial (and tangential) strains. The strains at the  $90^\circ$  location approached a constant strain value with increasing number of load application iterations. Despite the noted differences in the predicted growth, the two reference cases produced nearly identical axial, normal and tangential strains for each load application iteration at the surface locations studied. Thus, the two reference types used converted the same strain distributions into different amounts of growth.

#### 4.2 Phase 2: comparison of model driver measures

The shape changes resulting from individual and combinations of axial, torsional, bending, and surface loads (Figs. 1a–1f) and predicted by the current strain tensor based model with a range reference were quite similar to those predicted by published works using a von Mises based model and point reference [11], and a strain energy density based model and a range reference [23] despite differences in geometry, mesh, boundary conditions and reference threshold values. Because each of the models compared used arbitrary and different loading values, reference values, and stopping criteria, quantitative comparisons between resulting geometries for the three model types are difficult and unreliable. Instead, qualitative comparisons are presented based on visual observations

of the figures as well as the written descriptions reported in the referenced works [11] and [23] and on the geometries resulting from the current study. Figure 5 shows the initial and final shapes of the mid-cylinder cross-sectional geometry under the loading modes investigated using the developed strain tensor based model.

##### 4.2.1 Axial load

*Strain tensor based model* For the parameters chosen in this study, a uniform compressive load (Fig. 1a) applied along the cylindrical axis produced a uniform amount of growth along both the outer surface and the inner surface, resulting in an increased wall thickness, as shown in Fig. 5a.

*Strain energy density based model* In the SED based model study [23], the authors noted similar observations: “The axial loading history produced a uniform stimulus throughout the cross-section, resulting in uniform apposition on both surfaces.”

*von Mises stress based model* For the parameters chosen in the von Mises stress based model study [11], the authors of that study also reported a “constant stress distribution in any cross-section of the cylinder” and observed that this would result in a “constant growth and bone apposition” on both inner and outer surfaces. They further stated that either growth or shrinkage could occur depending on the magnitude of the reference value in relation to the magnitude of the stress at the cross-section.



#### 4.2.2 Torsional load

*Strain tensor based model* Given the chosen model parameters, a pure torsional load applied to an initially circular cylinder (Fig. 1c) also produced a constant effect over the outer and inner surfaces of the cylinder at each cross-section. In the case studied, the outer surface grew and the inner surface decayed, both uniformly at each cross-section (Fig. 5b).

*Strain energy density based model* For the parameters chosen in the SED based model study [23], “shear stresses that increased linearly through the thickness” were noted to cause “uniform periosteal apposition... and uniform endosteal resorption”.

*von Mises stress based model* For the parameters chosen in the von Mises stress based model study [11], similar observations were also reported. Again, these authors noted that the direction of the growth at each surface was dependent upon the surface von Mises stress value in relation to the reference von Mises stress value. They noted that, depending on the relative values, one of three cases would occur: (1) “significant swelling at the outer wall and a lesser swelling on the inner wall”, (2) “swelling ... at the outer circumference and shrinkage at the inner circumference”, or (3) “shrinkage at the inner and outer wall”.

#### 4.2.3 Bending load

*Strain tensor based model* Under pure bending (Fig. 1b) for the parameters chosen in the current strain tensor based model, a geometry symmetrical about the two Cartesian planes normal to each cross-section was produced with growth in the region of maximum stress and decay along the neutral axis on both the inner and outer surfaces, as shown in Fig. 5c. This is the loading condition used in Phase 1 of this study concerning reference type, the results of which were presented in Sect. 4.1.

*Strain energy density based model* For the parameters chosen in the SED based model study [23], the authors of that study noted “bone material was concentrated in the regions subjected to the highest bending stresses, primarily through periosteal apposition. The cortical thickness was reduced along the central, least stimulated (or ‘most neutral’) axis, primarily due to endosteal resorption.”

*von Mises stress based model* For the parameters chosen in the von Mises stress based model study [11], again, similar trends were noted. This model produced growth both on the inner and outer surfaces at the region of highest stress and decay on both surfaces along the neutral axis.

Combinations of these basic loading modes in Figs. 1a–1c produced less symmetrical shapes. Because of the increased complexity and variation in the application of the combined loading modes among the models compared, greater variation in the final geometries developed. However, as with the more basic loading modes, all three models produced similar growth trends.

#### 4.2.4 Axial + bending loads

*Strain tensor based model* Under the combination of axial compressive and bending loads (Fig. 1d), for the model parameters chosen, the shape generated was similar to that of the pure bending. However, more growth occurred on the compressive side of the bending moment and less growth occurred on the tensile side of the bending moment (Fig. 5d). The resulting geometry was symmetrical with respect to only one of the two planes indicated for pure bending, with one region of the outer surface having a larger amount of growth. The geometry produced is similar to the shapes due to the growth observed in noted experimental studies where animal bones were subjected to combined compressive and bending loads [7, 41, 42].

*Strain energy density based model* For the parameters chosen in the SED based model study [23], similar shape changes were produced where “bone was added on the more highly stressed ‘compressive side’ of the cross section ... and cortical thinning was produced on the less stressed ‘tension side’.”

*von Mises stress based model* The von Mises stress based model study [11], likewise, produced a similar geometry. For the parameters chosen by those authors, the shift of the neutral axis towards the “tension side” is visible through a region of slightly increased decay on the outer surface.

#### 4.2.5 Axial + bending + torsional loads

*Strain tensor based model* Including a torsional load to the combination of axial compression and bending

(Fig. 1e) resulted in the addition of a uniform growth over the entire inner and outer surfaces, as shown in Fig. 5e. This uniform growth added to the geometry resulting from the axial + bending loads described in Sect. 4.2.4 reduced the variation in wall thickness within the cylindrical geometry that developed from the axial and bending loads without torsion, for the chosen model parameters.

**Strain energy density based model** The SED based model study [23], noted that the inclusion of the torsional load drove “irregular cross-sectional geometries towards axisymmetry”. A “smoother endosteal contour and less cortical thinning on the tensile side” was observed.

**von Mises stress based model** The von Mises stress based model study [11] concluded that the addition of the torsional load to the combined axial and bending loads results in a more “oval structure”, as was noted for the strain-based and SED-based studies.

#### 4.2.6 Bending + torsion + surface forces

The final case studied was based on a combination of loading more representative of typical forces acting on a bone, including those induced by the muscles (Fig. 1f). Such loading was presented in only one of the published references [11] used for comparison to the current developed model. No axial compression was considered. Instead, the bending and torsional loads were combined with four localized surface loads applied on the outer surface of the cylinder and centered about the neutral axis of the bending moment as shown in Fig. 1f. Following [11] so that a direct comparison could be made, the positions of these localized loads were evenly spaced along the length of the cylinder. While their locations are not based on anatomy, the localization of surface loads simulate the forces of individual muscles acting through tendons attached to the bone. The regional surface forces resulted in localized regions of significant growth as shown in Fig. 5f. These localized regions of growth are easily visible in the three-dimensional geometry resulting from this combination of loading modes that is shown in Fig. 6.

While the model did not turn an initially circular cylinder to an anatomical three-dimensional bone shape, this was not the intention of the study since the loading and boundary conditions were not intended

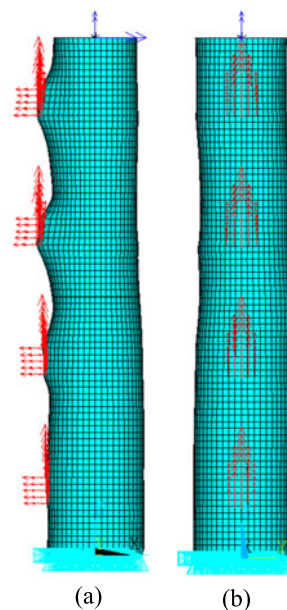


**Fig. 6** 3-D final geometry: bending + torsion + surface force. (a) X-Z view, (b) Y-Z view

to simulate specific physical activities. The resulting geometry does show the ways in which the volume’s shape would change to move the strains along the inner and outer surfaces towards a predefined reference value or range, thus reducing the strain variation over the surface. The correlations between model-predicted features and geometric features in actual bones may indicate that a bone’s adaptive behavior may be driven towards a similar goal.

At the midplane of the cylinder away from applied loads, the combination of bending, torsion and the local muscle surface forces produced an asymmetrical geometry. This asymmetry is also noted when observing the cross-sectional geometry of actual femur bones [25, 26]. It was not, however, predicted in the published results of the von Mises stress based model for the same loading conditions [11]. The von Mises stress based study in [11] showed that the asymmetrical geometry about the neutral bending axis could only be produced by the application of an asymmetric surface force, offset from the longitudinal symmetry plane (neutral bending axis). This is likely because the von Mises stress based model averages the strain tensor components to drive the shape changes, and, therefore, cannot be influenced by the differences in and variations of the individual component that drive the strain-tensor based model.

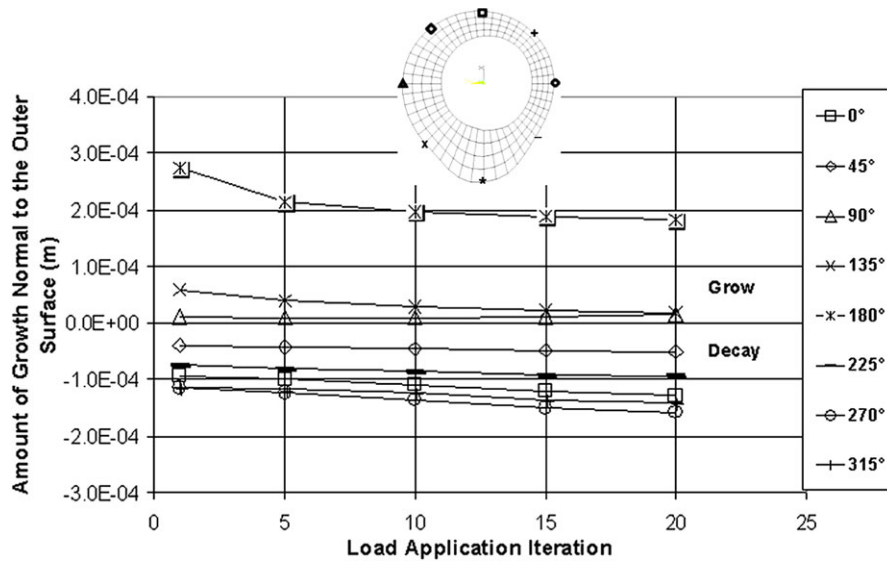


Fig. 7 Trends in amount of normal growth with load application iteration at discrete points on outer surface

Because this final combination of loading modes produced the most unique changes in shape, further analyses were performed to better understand how these loading conditions produced the observed shape changes under a strain tensor based model. Given in Fig. 7 is the growth at each load application iteration for discrete points on the outer surface at the cylindrical mid-plane at 45° increments. Trends in amount of growth with iteration were correlated to plots of the strain tensor values at some of these nodes shown in Fig. 8.

The applied regional surface forces were symmetrically centered about the  $\Theta = 180^\circ$  location, given that the  $x$ -axis corresponds to the  $\Theta = 0^\circ$  location (refer to Fig. 1 for Cartesian coordinate directions). The large radial-axial shear strains induced locally by the surface force as shown in Fig. 8a resulted in a large amount of growth at the  $180^\circ$  location, which approached a steady state rate with load application iteration, as shown in Fig. 7. The  $\Theta = 135^\circ$  and  $\Theta = 90^\circ$  locations were the only other locations to show growth, as indicated by their positive values in Fig. 7. At these locations, axial normal strain from the bending and radial-tangential shear strain from the torsion dominate, as shown in Fig. 8b and c.

Decay (negative growth) was observed at the remainder of the discrete locations studied on the outer surface at the midplane of the cylinder. At some locations, such as at  $\Theta = 225^\circ$  in Fig. 8d, decay is

expected as all strain tensor components lie in the “decay” range of strain values. In other locations, however, such as the  $45^\circ$  point in Fig. 8e, the net reduction in radius is not as obvious. In these locations, some strain tensor components, such as the axial normal strain and the radial-tangential shear strain have magnitudes which would contribute to local growth. However, many of the other strain tensor components, especially the axially directed shear strains, are near zero and are, therefore, midway between the two decay threshold values. Because the strain tensor based model used in this study summed equally weighted effects of all six strain tensor components, even if the component had near-zero values, these near-zero shear strains had a greater difference from the chosen, non-zero threshold values than did the non-zero strain tensor components at these same locations. Thus, while the net effect of the non-zero strains tensor components induced by the applied loads was positive growth, the total net effect of all the strain components, including the near-zero shear strain values, was negative and material removal occurred. It is the near-zero shear strain component values that appeared to be driving the decay at such locations for the loading conditions and threshold values chosen in this model.

The effect of the circumferential smoothing on the amount of growth per iteration shown in Fig. 7 was also seen in the gradual transitions surrounding the region of high growth near the surface load (located at

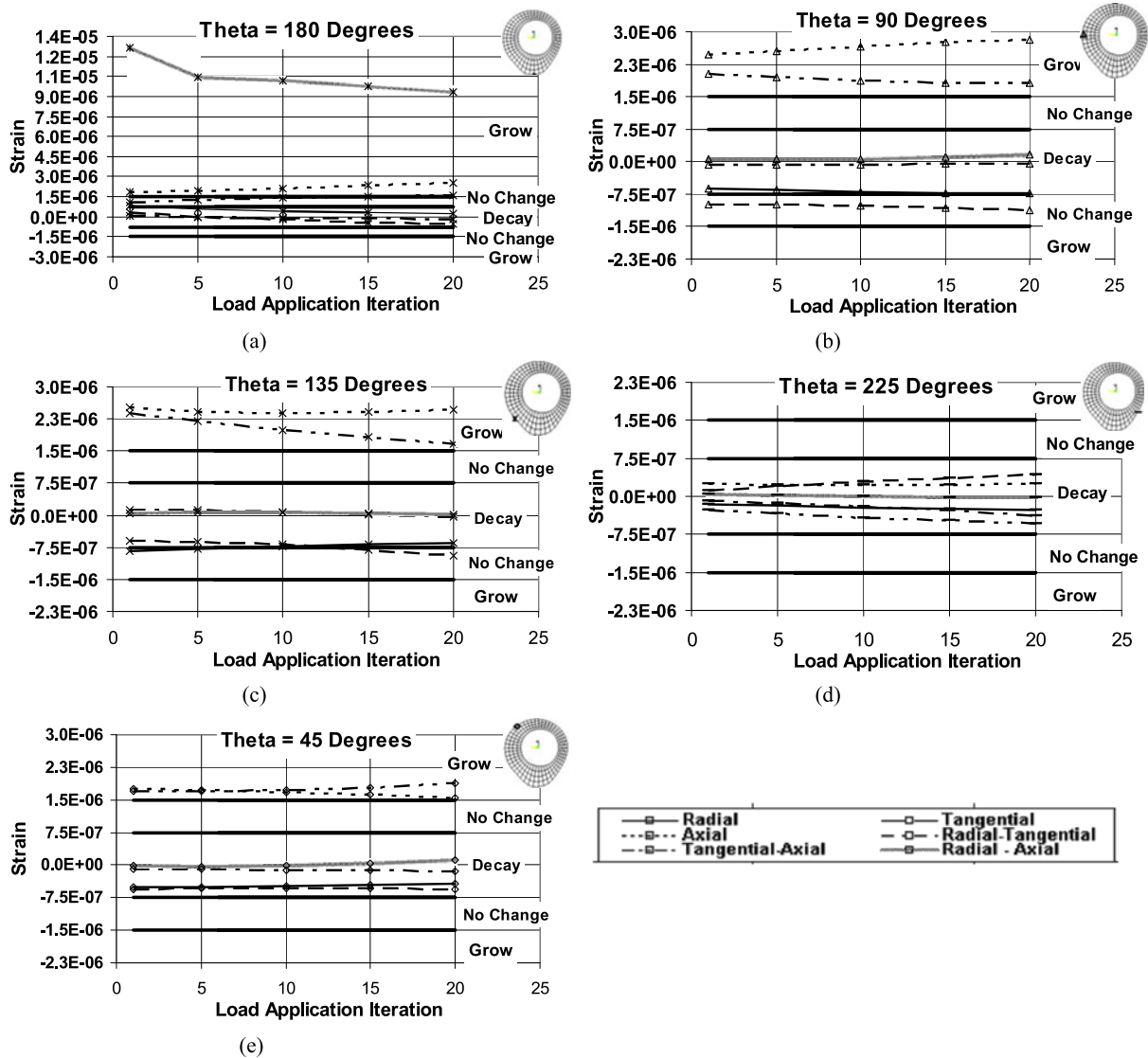


**Fig. 8** Trends in strain tensor component with load application iteration at discrete points on outer surface at theta locations. (a) 180°, (b) 90°, (c) 135°, (d) 225°, and (e) 45°

Theta = 180°) and its neighbors (located at Theta = 135° and Theta = 225°), despite the significant differences in the radial strain tensor component values at these points as shown in Fig. 8a, c, and d.

### 5 Discussion

#### 5.1 Phase 1: point vs range reference

Both point and range reference values in the strain tensor driven model produce similar trends in relative re-

gions of growth and decay. These trends also correlate well with those seen under the same boundary conditions and geometry reported in the published von Mises stress driven model with a point reference in [11], which was used for comparison. Slight differences in the amounts of growth between the two reference type models may be due to a number of reasons.

A likely cause is the choice of the selected reference threshold values. The difference between the strain tensor component value and the reference threshold value(s) is directly related to the amount of growth

predicted at each load application iteration. In general, the point reference showed a larger difference between the nodal strain values (which were nearly the same regardless of the reference type used) and the reference values, as threshold values in the reference range case were  $\pm 50\%$  those of the point reference case. This typically resulted in the greater amount of growth observed in the point reference case at each iteration at the nodal locations compared. Because growth per iteration is then summed over the total number of iterations run to create the final geometries, the resulting images used for comparison in Fig. 3 were achieved in fewer iterations for the point reference model, which had a greater amount of growth per iteration. However, because of this cumulative effect, and because neither model reached a steady state growth at the comparison point chosen by visual inspection of the shape change, the total number of iterations performed also affected the quantitative comparison of radial change in Table 3.

The differences in local shape changes due to these phenomena were then propagated away from each node to neighboring nodes due to the cumulative effect of the surface smoothing performed, resulting in more significant shape changes than what would be indicated by nodal strain values alone. Surface smoothing, however, was found to be beneficial and necessary to ensure that locally high strains did not produce large regional discontinuities in growth along each surface and to ensure that the mesh integrity was intact during the entire analysis.

Because the strain tensor based growth model used in this phase of study sums the individual effects of the strain tensor components, the influence of each strain tensor component on the trends in growth can be identified. For example, the discontinuity in the trend of the growth per iteration with iteration number on the inner surface in the model using the reference range (Fig. 4a) can be explained by the relative values of the radial, tangential and axial strain and their respective reference values. As seen in Fig. 4c axial strains do not enter the “growth region” until the last 40 load application iterations. At this same time, the radial and tangential strain values driving the decay approach the reference range threshold, and enter the “lazy zone” or “equilibrium range”. Thus, the axial strains begin to dominate the shape changes in this region, resulting in the abrupt change in amount of growth at the node examined. The point reference type model

does not experience these abrupt changes because this model does not encounter a range of strains producing no shape changes between designated growth-creating and decay-creating strain values.

Despite the differences in the model function inherent in the choice of reference type that have been discussed, this analysis showed that the reference type used does affect the amount of the shape changes with each load application and the number of load applications needed to achieve a certain amount of growth at a particular location. The choice of reference type does not, however, significantly affect the distribution of the shape changes over the surfaces. Thus, a model with a singular point reference type and a model with a reference range type whose threshold values are  $\pm 50\%$  of the value used in the point reference type model, produce similar trends in shape change under the same loading conditions. It is possible, however, that as the span of the reference range deviates more from the point reference value, such as through the selection of different threshold values than what were used in this study, the differences in amount of shape change with location may increasingly vary from the point reference case and may result in more significant dissimilarities in shape.

## 5.2 Phase 2: comparison of model driver measures

With the proper selection of the relationships between the applied load and reference values, the strain tensor based, von Mises stress based, and the strain energy density based models compared here all predicted quite similar shape changes as a result of basic applied loading modes and their combinations. This is despite the significant differences in actual values of these parameters and methods of applying the loads, developing the finite element models, and executing the shape prediction models. As has been noted by other authors [13, 14, 43], it is clear that the magnitude and direction of the surface change can be altered through variations in the relationship between values of the applied load and the reference threshold values.

The reasoning behind the choice of specific reference values varied for each model. In many numerical shape adaptation models, the selection of the reference values or reference range values, especially in relation to the loading conditions, is arbitrary and chosen to produce expected shapes, such as those observed experimentally [20, 30].



In the simulations used in this comparison, the selected reference values were related to the selected loading values. The von Mises stress-based model in [11] chose a reference value equal to the average von Mises stress generated by the applied load for the basic loading modes. The strain energy density based model in [23] chose the reference range to be 30–70 % of the applied load for the basic loading modes. The authors of that strain energy density based study acknowledged that this relationship was not followed for the mixed mode loading, though the exact alternative relationship was not disclosed.

For the strain tensor based model developed for the present investigation, a number of preliminary studies were performed in order to determine appropriate reference threshold values. In this current model, equal reference threshold values were preferred for each strain tensor component in order to reduce the model's dependency on geometric orientation and strain tensor component type. However, to achieve some of the shapes presented here, this was not always possible, as seen in the different reference ranges chosen for the pure axial compression and the bending + torsion + surface force loading cases listed in Table 2. While the variations in reference threshold values with loading mode seem to be arbitrary, it has been thought that the actual reference threshold values of bone cells may vary not only with loading mode (e.g. shear vs. normal) but also with location along the surfaces of the bone to correspond with variations in the "typical" loads encountered along the surfaces of the bones [12]. The use of different reference ranges, however, may create difficulty when applying these types of models to compare the effects of loading modes for which there may be no experimental or reference shapes to use for validation.

The use of a shape modification model based on individual strain tensor components allows for a better understanding of the direct influence and contribution of each strain tensor component on the resulting alterations in the bone surface profile. This was illustrated in the analysis of the contributions of the individual components to the growth at discrete points along the bone surfaces (Fig. 8) explained in Sect. 4.2. While von Mises stress and strain energy density are averaged measures that summarize the effects of the applied load at each surface point subjected to growth or decay, the specific stress/strain components cannot be deduced from the values of these averaged measures. Through a strain tensor based model, it is easy

to see which strain components are the main drivers of the shape changes observed. However, the strain tensor based model is dependent upon the orientation of the coordinate systems used to obtain the tensor components, and care must be taken to ensure that the reference threshold values refer to the same system definition. This may reduce its ability to be used as a generalized modeling and analysis tool, especially in a multi-bone system.

## 6 Conclusions

Numerical models to predict cortical bone strength adaptation through the modifications of bone shape with variations in load, such as those developed and analyzed in the current work, can provide insight into the load-growth relationship that may be difficult to obtain experimentally or clinically. A wide variety of modeling methods and driving measures have been used in predicting bone shape adaptation. This study has shown that, with the proper selection of model parameter values, these significantly different numerical models can produce quite similar shape predictions. This knowledge might be useful in the development of a model to predict shape changes under a single loading mode that has been studied experimentally or clinically in order to aid in the understanding of the phenomena observed. However, to be able to use numerical modeling and simulation tools to compare the changes in bone strength resulting from various loading modes, less sensitivity to the reference frame in the calculation of model driver measures and to the selection of model parameters, such as the reference values, might be necessary. Hence, further investigation into the development of alternative approaches to modeling bone shape adaptation due to mechanical loading is warranted.

**Acknowledgements** This work was partially supported by an Amelia Earhart Fellowship from the Zonta International Foundation.

## References

1. Martin RB, Burr D (1989) Structure, function and adaptation of compact bone. Raven Press, New York
2. Dequeker J (1971) Periosteal and endosteal surface remodeling in pathologic conditions. *Invest Radiol* 6(4):260–265

3. Currey JD (2002) *Bones: structure and mechanics*. Princeton University Press, Princeton
4. Hart RT, Davy DT, Heiple KG (1984) A computational method for stress analysis of adaptive elastic materials with a view toward applications in strain-induced bone remodeling. *J Biomech Eng* 106(4):342–350
5. Cowin SC, Hart RT, Balsler JR, Kohn DH (1985) Functional adaptation in long bones: establishing in vivo values for surface remodeling rate coefficients. *J Biomech* 18(9):665–671
6. Huiskes R, Weinans H, Grootenboer HJ, Dalstra M, Fudala B, Slooff TJ (1987) Adaptive bone-remodeling theory applied to prosthetic-design analysis. *J Biomech* 20(11–12):1135–1150
7. Brown TD, Pedersen DR, Gray ML, Brand RA, Rubin CT (1990) Toward an identification of mechanical parameters initiating periosteal remodeling: a combined experimental and analytic approach. *J Biomech* 23(9):893–897
8. Van der Meulen MCH, Beaupre GS, Carter DR (1993) Mechanobiological influences in long bone cross-sectional growth. *Bone* 14:635–642
9. Chen G, Pettet GJ, Pearcy M, McElwain DLS (2007) Modelling external bone adaptation using evolutionary structural optimisation. *Biomech Model Mechanobiol* 6(4):275–285
10. Annicchiarico W, Martinez G, Cerrolaza M (2007) Boundary elements and [beta]-spline surface modeling for medical applications. *Appl Math Model* 31(2):194–208
11. Mittlmeier T, Mattheck C, Dietrich F (1994) Effects of mechanical loading on the profile of human femoral diaphyseal geometry. *Med Eng Phys* 16(1):75–81
12. Cowin SC, van Buskirk WC (1979) Surface bone remodeling induced by a medullary pin. *J Biomech* 12(4):269–276
13. Cowin SC, Firoozbakhsh K (1981) Bone remodeling of diaphyseal surfaces under constant load: theoretical predictions. *J Biomech* 7:471–484
14. Cowin SC (1987) Bone remodeling of diaphyseal surfaces by torsional loads: theoretical predictions. *J Biomech* 20(11–12):1111–1120
15. Lanyon L (1987) Functional strain in bone tissue as an objective, and controlling stimulus for adaptive bone remodeling. *J Biomech* 20:(11/12):1083–1093
16. Gross TS, Edwards JL, McLeod KJ, Rubin CT (1997) Strain gradients correlate with sites of periosteal bone formation. *J Bone Miner Res* 12(6):982–988
17. Judex S, Gross TS, Zernicke RF (1997) Strain gradients correlate with sites of exercise-induced bone-forming surfaces in the adult skeleton. *J Bone Miner Res* 12(10):1737–1745
18. Xu W, Robinson K (2008) X-ray image review of the bone remodeling around an osseointegrated trans-femoral implant and a finite element simulation case study. *Ann Biomed Eng* 36(3):435–443
19. Koontz JT, Charras GT, Guldborg RE (2001) A microstructural finite element simulation of mechanically induced bone formation. *J Biomech Eng* 123(6):607–612
20. Kumar NC, Dantzig JA, Jaisuk IM, Robling AG, Turner CH (2010) Numerical modeling of long bone adaptation due to mechanical loading: correlation with experiments. *Ann Biomed Eng* 38(3):594–604
21. Adams DJ, Spirt AA, Brown TD, Fritton SP, Rubin CT, Brand RA (1997) Testing the daily stress stimulus theory of bone adaptation with natural and experimentally controlled strain histories. *J Biomech* 30(7):671–678
22. Tekkaya AE, Guneri A (1996) Shape optimization with the biological growth method: a parameter study. *Eng Comput* 13(8):4–18
23. Levenston ME, Beaupre GS, Carter DR (1998) Loading mode interactions in simulations of long bone cross-sectional adaptation. *Comput Methods Biomech Biomed Eng* 1:(4):303–319
24. Carter DR, van der Meulen MCH, Beaupre GS (1996) Mechanical factors in bone growth and development. *Bone* 18(1):5S–10S
25. Martin RB, Atkinson PJ (1977) Age and sex-related changes in the structure and strength of the femoral shaft. *J Biomech* 10:223–231
26. Martens M, Van Audekercke R, De Meester P, Mulier JC (1981) The geometrical properties of human femur and tibia and their importance for the mechanical behaviour of these bone structures. *Arch Orthop Trauma Surg* 98(2):113–120
27. ANSYS Inc. ANSYS. 11.0. Canonsburg
28. Abd-Alla A, Abo-Dahab S, Mahmoud S (2011) Wave propagation modeling in cylindrical human long wet bones with cavity. *Meccanica* 46(6):1413–1428. doi:10.1007/s11012-010-9398-5
29. Lieberman DE, Polk J, Demes B (2004) Predicting long bone loading from cross-sectional geometry. *Am J Phys Anthropol* 123:156–171
30. Roberts MD, Hart RT (2005) Shape adaptation of long bone structures using a contour based approach. *Comput Methods Biomech Biomed Eng* 8(3):145–156
31. Batina JT (1990) Unsteady Euler airfoil solutions using unstructured dynamic meshes. *AIAA J* 28(8):1381–1388
32. Papini M, Zdero R, Schemitsch EH, Zalzal P (2007) The biomechanics of human femurs in axial and torsional loading: comparison of finite element analysis, human cadaveric femurs, and synthetic femurs. *J Biomech Eng* 129(1):12–19
33. Heiner AD, Brown TD (2001) Structural properties of a new design of composite replicate femurs and tibias. *J Biomech* 34:773–781
34. Cristofolini L, Viceconti M, Cappello A, Toni A (1996) Mechanical validation of whole bone composite femur models. *J Biomech* 29(4):525–535
35. Dennis MG, Simon JA, Kummer FJ, Koval KJ, DiCesare PE (2000) Fixation of periprosthetic femoral shaft fractures occurring at the tip of the stem: a biomechanical study of 5 techniques. *J Arthroplast* 15(4):523–528
36. Szivek JA, Weng M, Karpman R (1990) Variability in the torsional and bending response of a commercially available composite “Femur”. *J Appl Biomater* 1(2):183–186
37. Mullender MG, Huiskes R, Weinans H (1994) A physiological approach to the simulation of bone remodeling as a self-organizational control process. *J Biomech* 27(11):1389–1394
38. Hirose S, Li M, Kojima T, de Freitas PHL, Ubaidus S, Oda K, Saito C, Amizuka N (2007) A histological assessment on the distribution of the osteocytic lacunar canalicular system using silver staining. *J Bone Miner Metab* 25:374–382

39. Pazzaglia UE, Congiu T, Raspanti M, Ranchetti F, Quacci D (2009) Anatomy of the intercortical canal system: scanning electrode microscopy study in rabbit femur. *Clin Orthop Relat Res* 467(9):2446–2456
40. Kamioka H, Honjo T, Tankano-Yamamoto T (2001) A three-dimensional distribution of osteocyte processes revealed by the combination of confocal laser scanning microscopy and differential interface contrast microscopy. *Bone* 28(2):145–149
41. Liskova M, Hert J (1971) Reaction of bone to mechanical stimuli. Part 2. Periosteal and endosteal reaction of tibial diaphysis in rabbit to intermittent loading. *Folia Morphol (Praha)* 29(3):301–317
42. Lanyon LE, Rubin CT (1984) Static vs dynamic loads as an influence on bone remodelling. *J Biomech* 17(12):897–905
43. Guo X-D, Cowin SC (1992) Periosteal and endosteal control of bone remodeling under torsional loading. *J Biomech* 25(6):645–650